Numerical Analysis of Transient Vortex Formation at the Outlet of a Tank Containing Gas-Liquid Phases

M. Mohseni[1†] and M. K. Domfeh[2]

[1] Department of Mechanical Engineering, Qom University of Technology, Qom 37181 46645, Iran
[2] Earth Observation Research and Innovation Centre (EORIC), University of Energy and Natural Resources, P. O. Box 214, Sunyani, Ghana

†*Corresponding Author Email: m.mohseni@qut.ac.ir*

ABSTRACT

One of the basic phenomena when a liquid leaves a tank is the formation of vortices. This phenomenon can have a significant impact on the liquid mass remaining in the tank and the ingress of air and bubbles into the system. As a result, the performance of the system can be disturbed. The purpose of this study is to numerically investigate the effect of gas pressure on vortex formation and critical height. It also verifies the relationships presented for turbulent viscosity. In addition, the near-wall behavior of the analytical relationships proposed for the tangential velocity is revised based on the boundary layer theory. Some common effective factors such as angular velocity, discharge time, and liquid height are also investigated. The volume of fluid (VOF) model and the Transitional SST k-ω turbulence model were used to solve the two-phase turbulent flow. The results show that increasing the gas pressure from 1 to 5 bar and its direct impact on the liquid surface significantly accelerates the formation of the vortex and the critical height. This phenomenon causes the air core to reach the inlet of the outlet pipe approximately 7 seconds earlier after the start of the liquid discharge. As a result, much more liquid mass remains in the tank. The increase in the angular velocity of the reference frame from 0.1 to 1 rad/s also causes the critical height to be reached much earlier and the remaining liquid mass to increase by 32 kg. In addition, the amount and variations of turbulent viscosity differ significantly from the semi-empirical constants, limiting their use to certain flows.

1. INTRODUCTION

Gas-liquid two-phase flow exists in many industrial applications, including liquid fuel tanks (Karimi et al., 2010, Li et al., 2019). In these tanks, the two gas and liquid phases are juxtaposed until the end of the engine operation (Li et al., 2019; Zuo et al., 2021). In fact, a pressurized gas supply system is required to pressurize the fuel and oxidizer in the propellant tanks and transfer them to the combustion chamber at the required flow and pressure. The outflow of liquid propellant from the tanks is associated with the formation of vortices (Agarwal et al., 2104). Other examples are the air-core vortex in the turbine inlet in the upstream tank of a hydroelectric power plant, the pump inlet in a pumping system, or generally in front of hydraulic inputs (Suerich-Gulick1 et al., 2014; Zi et al., 2021).

The vortex phenomenon has in some cases destructive effects on system performance, such as reduced flow, reduced efficiency of hydraulic machines (pumps and turbines), noise production, harmful vibrations, and damage or corrosion of components (Trivellato, 2010; Jochmann et al., 2006; Kabiri-Samani & Borghei, 2013; Agarwal et al., 2014; Suerich-Gulick1 et al., 2014; Wang et al., 2011) and/or instability of hydraulic machines (Zi et al., 2021; Kan et al., 2023). Delaying the time of vortex formation can be an important step to improve system performance. In some cases, a vortex breaker or anti-vortex plate is used to prevent or reduce the strength of the vortex (Jochmann et al., 2006; Trivellato, 2010). In general, the reasons for vortex formation are (Agarwal et al., 2104; Trivellato, 2010):

1. Asymmetric geometry at boundaries.

2. Asymmetric flow as it approaches the outlet.

NOMENCLATURE			
d	Pipe diameter (m)	α	Volume fraction
k	Turbulent kinetic energy (m^2/s^2)	γ	Fluid thermal conductivity (W/m.K)
p	Fluid pressure (Pa)	Γ	Circulation (m^2/s)
Q	Volume flow rate (m3/s)	ε	Dissipation rate of turbulent kinematic energy (m^2/s^3)
r	Radius (m)	θ	Tangential direction in cylindrical coordinates
r_m	Radius at maximum tangential velocity (m)	μ	Dynamic viscosity (kg/m.s)
$\bar{r}$	Dimensionless radius (r/r_m)	μ_t	Turbulent viscosity (kg/m.s)
R	Local tank radius (m)	ν	Kinematic viscosity (m^2/s)
$\bar{R}$	Dimensionless radius (r/R)	ρ	Fluid density (kg/m3)
t	Time (sec)	Ω	Angular velocity (rad/s)
T	Temperature (K)	ω	Specific dissipation rate in k- ω turbulence model (m^2/s^3)
v, u	Velocity components (m/s)		
V_θ	Tangential velocity (m/s)		
$V_{\theta m}$	Maximum tangential velocity (m/s)		
z	Longitudinal coordinates of the tank (m)		

3. Non-uniform velocity distribution due to boundary layer separation (flow regime instability).

4. Effect of ground Coriolis force and the presence of pre-rotation before fluid discharge.

So far, many efforts have been made to solve the problems related to vortex formation, even in recent years (Zi et al., 2021, 2022; Kan et al., 2023). Many researchers have attempted to provide analytical relationships for the velocity components and critical height in a vortex stream by simplifying the mass continuity and Navier-Stokes equations (Odgaard, 1986; Wang et al., 2011). Given the advantages of analytical solutions, efforts have been made to do so even recently (Sun & Liu, 2015; Azarpira & Zarrati, 2019). However, in cases where the fluid container has a significant deviation from the axisymmetric state, or the inputs and outputs are not in the same direction, or the vortex breaker is installed, these relationships will not be able to accurately predict the flow behavior.

In parallel with the analytical work, many attempts have been made through experiments and numerical simulations. In general, these studies investigate some phenomena and topics, such as the formation of vortices in specific geometries, for example in tanks and turbines, the details of vortex formation, such as critical height, velocity components, and structure of vortices (Basu et al., 2013; Agarwal et al., 2104; Naderi et al., 2019; Zi et al., 2020), improved analytical relationships (Sun & Liu, 2015; Azarpira & Zarrati, 2019), the effect of important dimensionless numbers such as Reynolds, Weber, and Froude (Taştan & Yildirim, 2014; Mahyari et al., 2010), the effect of the vortex breaker and its shape (Jochmann et al., 2006; Mahyari et al., 2010; Trivellato, 2010; Monshizadeh et al., 2018), the use of the vortex for thermal energy transfer (Tayyab et al., 2020), and sometimes a comparison between the performance of turbulence models (Mulligan et al., 2014; Huang et al., 2017; Domfeh et al., 2020a). Due to the complexity of the problem, almost all numerical simulations have been performed using commercial software such as Ansys Fluent (Mahyari et al., 2010), Ansys CFX (Agarwal et al., 2014; Mulligan et al., 2014; Ahn et al., 2019), Flow 3D (Azarpira & Zarrati, 2019; Huang et al., 2017; Sarkardeh,

2017), and open source CFD codes such as OpenFOAM (Domfeh et al., 2020a). Another powerful software capable of solving complex phenomena such as heat transfer in supercritical fluids is Star CCM+ (Manda et al., 2020, 2021, 2022, 2023), which can also be used for vortex flows such as the present study (Thingbø, 2013).

Despite the good studies carried out so far, there is still a need for further research in this area, as pointed out by Domfeh et al., (2020b). Therefore, in addition to investigating the usual effective factors in vortex formation and critical height, such as angular velocity, discharge time, and liquid height, this study specifically investigates the effect of gas pressure on vortex formation and the validity of the relationships presented for turbulent viscosity in a turbulent vortex flow. It also aims to correct the near-wall behavior of the analytical relationships presented in the literature for tangential velocity profiles using boundary layer theory.

2. PROBLEM DESCRIPTION

The geometry studied is a symmetrical tank, shown schematically in Fig. 1. To illustrate the vortex parameters, the results are plotted at different cross-sections of the tank bottom, also shown in Fig. 1. The diameter of the inlet and outlet sections of the tank is 0.1 meters, the diameter of the central section is 0.7 meters and the total length of the tank is 1.7 meters.

Boundary conditions and fluid properties are given in Tables 1 and 2, respectively. Optionally, gas and liquid in the two-phase flow are considered air and water. The surface tension σ between air and water at normal temperatures is approximately 0.072 N/m. This value is used in the numerical simulation.

In this study, among the vortex-causing factors mentioned in the introduction, only the effects due to the rotation of the reference frame were considered. For this purpose, two rotation speeds of 0.1 and 1 rad/s are used. Also, to investigate the effect of air pressure on vortex formation, two pressures of 1 and 5 bar are considered. In addition, to create both laminar and turbulent flow regimes, the outflow rates are set to 0.3 and 3 kg/s
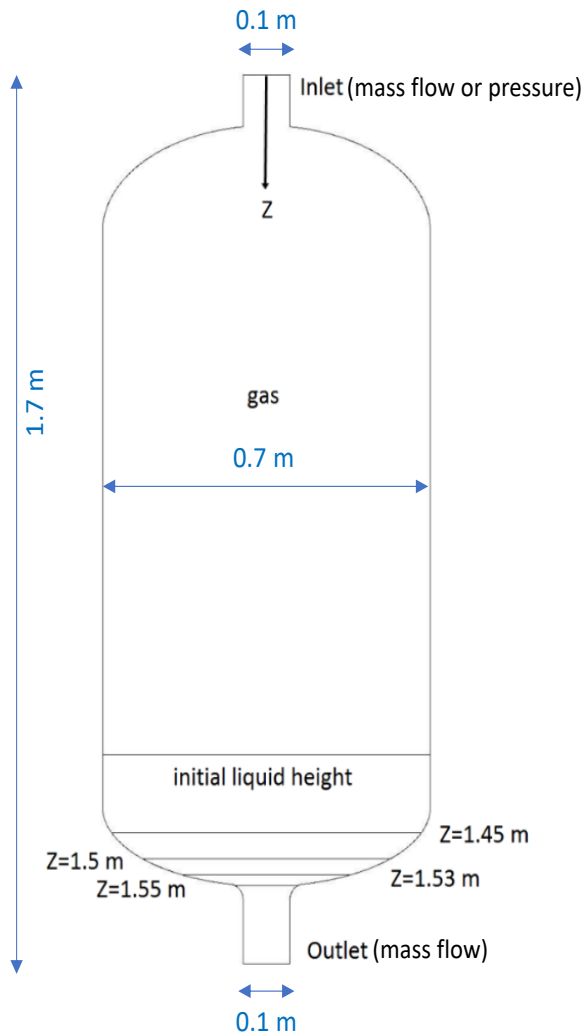
Fig. 1 Schematic of the tank and position of lines to display the results

Table 1 Boundary conditions

Boundry Type	Value or Type	Unit
Tank wall	insulation	---
Inlet gas temperature	300	K
Initial fluid temperature	300	K
Inlet mass flow rate	0.01, 0.0175	kg/s
Inlet pressure	1, 5	bar
Outlet liquid temperature	300	K
Outlet mass flow rate	0.3, 3	kg/s

Table 2 Water and air properties at pressure 101.325 kPa

Fluid	T (K)	ρ (kg/m³)	Cp (J/kg.K)	k (W/m.K)	μ (kg/m.s)
Water	300	998.2	4182	0.6	0.001001
Air	300	ideal gas	1006.43	0.0242	1.79×10^{-5}

respectively. Table 3 provides a summary of the solution conditions used in this study.

Table 3 Summary of the solution conditions

Run No.	Flow regime	Air pressure (bar)	Angular velocity (rad/s)	Liquid flow rate (kg/s)
Run1	Laminar	1	0.1	0.3
Run2	Laminar	1	1	0.3
Run3	Turbulent	1	0.1	3
Run4	Turbulent	1	1	3
Run5	Turbulent	5	1	3

The most important dimensionless numbers in the vortex flow study are the Reynolds number, Re=ρVd/μ, the Froude number, Fr=V/$\sqrt{gd}$, and the Weber number, We=ρV²d/σ, where the velocity and diameter are based on the inlet pipe (Odgaard, 1986; Hite & Mih, 1994). Accordingly, for two outlet mass flow rates of 3 and 0.3 kg/s, the values of the Reynolds number are 38197 and 3819.7, the values of the Froude number are 0.386 and 0.0386, and the values of the Weber number are 200 and 2, respectively. The circulation number, N_Γ=Γd/Q, can also be important in a free surface vortex flow. However, the value of Γ is not constant but a function of space and time for each flow condition.

3. MODELING PROCEDURE

The governing equations, the generation and independence of the mesh, and the solution method applied to the modeling of the two-phase vortex flow described in section 2 are discussed below.

3.1 Governing Equations

The governing equations include the mass continuity equation, the momentum and energy equations, the equations of the turbulence model, and the two-phase flow equations, which are presented below.

In this research, the VOF model was used to solve the two-phase flow. This model can simulate the behavior of two or more immiscible fluids and is more suitable for layered and free surface flows (Fluent 6.3 User's Guide, 2006). The basis of this model is that the volume fraction of all phases in each control volume is equal to one. The field variables and properties in each cell are common to all phases. Therefore, depending on the volume fraction of each phase, the properties in each control volume may belong to one phase or the whole (combination) of phases. This model has been used in almost all numerical simulations. The continuity equation for phase q is as follows (Fluent 6.3 User's Guide, 2006).

$$\frac{\partial}{\partial t}(\rho_q \alpha_q) + \nabla \cdot (\rho_q \alpha_q \boldsymbol{V}) = 0 \qquad (1)$$

The volume fraction equation for the first phase is not solved but is obtained from the following condition.

$$\sum_{q=1}^{n} \alpha_q = 1 \qquad (2)$$

The phases determine the properties in the transfer equations in each control volume. For example, in a two-phase system, if the phases are denoted by indices 1 and 2, then the density in each cell is determined by the following

relationship (the volume fraction of the second phase is followed).

$$\rho = \alpha_2 \rho_2 + (1 - \alpha_2)\rho_1 \qquad (3)$$

Other properties, such as viscosity, are calculated in the same way. In a two-phase flow model, a momentum equation is solved over the entire field, and the resulting velocity field is divided between the phases. The momentum equation depends on the volume fraction of all phases through their viscosity and density and is defined for turbulent flows as follows

$$\frac{\partial(\rho \boldsymbol{V})}{\partial t} + \nabla \cdot (\rho \boldsymbol{V}\boldsymbol{V}) = \rho \boldsymbol{g} - \nabla p + \boldsymbol{\nabla}.(\tau + \tau_t) \qquad (4)$$

where

$$\tau = \mu[\boldsymbol{\nabla V} + (\boldsymbol{\nabla V})^T] - (2/3)\boldsymbol{\delta}\mu\boldsymbol{\nabla} \cdot \boldsymbol{V}$$

is viscous shear stress and

$$\tau_t = \mu_t[\boldsymbol{\nabla V} + (\boldsymbol{\nabla V})^T] - (2/3)\boldsymbol{\delta}(\rho k + \mu_t\boldsymbol{\nabla} \cdot \boldsymbol{V})$$

is turbulent shear stress, which is based on the Boussinesq hypothesis. The energy equation is also shared between the phases and is written as follows.

$$\frac{\partial}{\partial t}(\rho E) + \boldsymbol{\nabla} \cdot [\boldsymbol{V}(\rho E + p)] = \boldsymbol{\nabla} \cdot (\gamma \boldsymbol{\nabla} T) \qquad (5)$$

where E for each phase is obtained from the following equation.

$$E = \frac{\sum_{q=1}^{n} \rho_q \alpha_q E_q}{\sum_{q=1}^{n} \rho_q \alpha_q} \qquad (6)$$

Due to the good performance of the SST k-ω turbulence model, as reported by previous researchers (Basu et al., 2013; Huang et al., 2017; Ahn et al., 2019), this model was used to solve the turbulent flow. The equations for k (turbulent kinetic energy) and ω (specific dissipation rate) in this model are as follows (Versteeg & Malalasekera, 2007).

$$\begin{aligned} \frac{D(\rho k)}{Dt} = \frac{\partial}{\partial x_j}\left[\left(\mu + \frac{\mu_t}{\sigma_k}\right)\frac{\partial k}{\partial x_j}\right] + 2\mu_t S_{ij} \cdot S_{ij} \\ - \frac{2}{3}\rho k \frac{\partial U_i}{\partial x_j}\delta_{ij} - \beta^*\rho k\omega \end{aligned} \qquad (7)$$

$$\begin{aligned} \frac{D(\rho\omega)}{Dt} = \frac{\partial}{\partial x_j}\left[\left(\mu + \frac{\mu_t}{\sigma_\omega}\right)\frac{\partial\omega}{\partial x_j}\right] + 2\rho\gamma_2 S_{ij} \cdot S_{ij} \\ - \frac{2}{3}\rho\gamma_2\omega \frac{\partial U_i}{\partial x_j}\delta_{ij} - \beta_2\rho\omega^2 \\ + F \end{aligned} \qquad (8)$$

where

$$\mu_t = \frac{a_1\rho k}{max(a_1\omega, SF)} \qquad (9)$$

It should be noted that the SST k-ω turbulence model is a hybrid model which uses the standard k–ε model in the fully turbulent region far from the wall and the Standard k–ω model in the near-wall region (Versteeg & Malalasekera, 2007). This combination is due to the weakness of the two models in the mentioned regions, i.e., the standard k–ε model in the near wall region and the standard k-ω model in the regions far from the wall. In other words, the SST k-ω model uses the ability of both
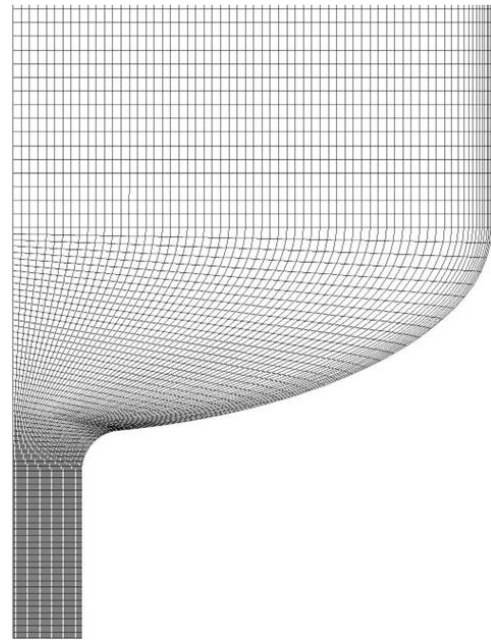

Fig. 2 Mesh produced to use the SST k-ω model (for better clarity, only the bottom of the tank is shown)

models in other regions. In addition, since some regions have a relatively low Reynolds number and the flow may be in the transitional regime between laminar and turbulent flows, the "Transitional Flows" option was applied along with the SST k-ω model to capture the low Reynolds number regions. By enabling this option, a low Reynolds number correction is applied to the turbulent viscosity.

3.2 Mesh generation and mesh independency

In this study, due to the advantages of the structured mesh, including the much smaller number of grids compared to the unstructured mesh, this type of mesh was used. The mesh generated is shown in Fig. 2.

An important issue in numerical simulation with CFD is mesh independency or grid study which means that the results do not change with increasing the number of grids. Since, the main parameter in the present study is the tangential velocity, the major criterion in the mesh study is the radial changes of this quantity. Fig. 3 shows the grid study for the flow conditions of Run 4. As can be seen, the numerical results are the same for grid numbers 25839 and 34963. Therefore grid number 25839 was used for further calculations. Care should also be taken with other flow conditions.

In addition to the type of mesh and grid study, when the SST k-ω turbulence model is used alongside the transitional flows in Fluent, the y+ at the wall-adjacent cell should be on the order of 1. However, a higher y+ is acceptable as long as it is well within the viscous sublayer (y+ < 4 to 5). Figure 4 shows the changes in y+ for run 3 as an example. In other words, when using the SST k-ω model, the equations are solved up to the wall. Therefore, this model requires a much higher mesh density than the high Reynolds number (HRN) models, such as the standard k-ε model.
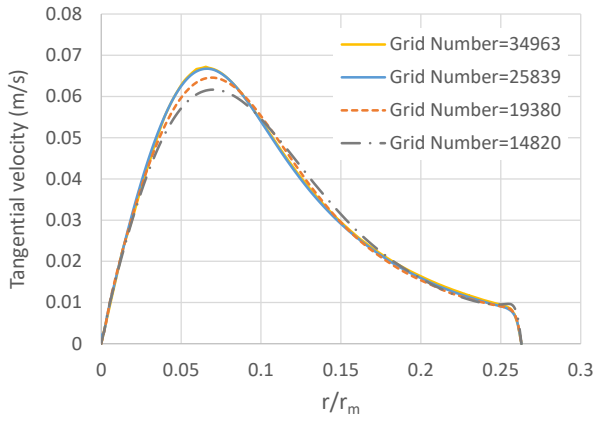
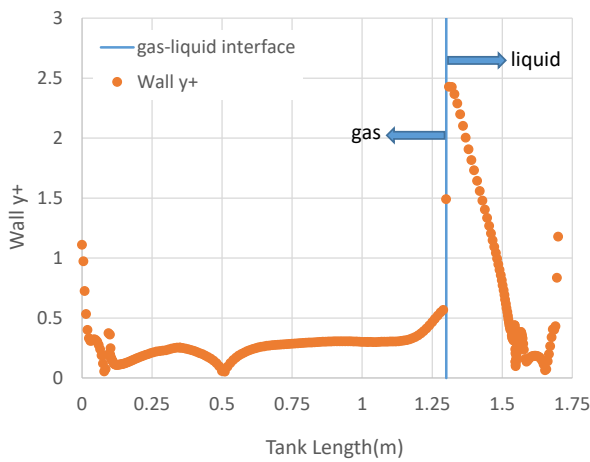**Fig. 3. Investigation mesh independency for the present study**

Fig. 4 A sample of wall y+ variations along the tank wall for Run3

3.3 Method of Solution

Due to the complexity of the vortex flow phenomenon, the numerical simulation was performed using the Fluent 6.3 CFD code. The solution was executed as axisymmetric due to the axial symmetry of the flow and to save computational time and cost. The finite volume method has been used for the numerical solution. The PISO algorithm was also used to solve the velocity and pressure coupling equations. This algorithm is more suitable for solving transient flow problems than existing algorithms (Versteeg & Malalasekera, 2007). The first-order upwind scheme is also used for convective terms in the momentum and turbulence equations. In addition, the solution convergence criterion for the various equations is at least 10^{-5}, except for the mass conservation equation, where the convergence value is set to 10^{-3}.

Given that in the present study, the formation of the vortex and the discharge of fluid from the tank is a transient problem, another essential parameter to be considered for convergence of the numerical solution is the time step size so that small values of the order of 10^{-3} and less must be applied. Even as time goes on or the solution conditions change, for example, increasing the air

pressure from 1 to 5 bar, smaller values of this quantity of the order of 10^{-5} should be used. In other words, it takes about 100,000 time-steps to complete 1 second. This small time step adds to the solution time, so that in some cases, such as Run5 in Table 3, even on a powerful home computer (32 Gig. RAM, CPU: Intel Core i7 8700k @ 3.70 GHz) and with Fluent's parallel capabilities enabled, solving the problem can take several days. It should be noted that in this study, to discretize the unsteady formulation the first-order implicit method has been used. In other words, no stability criterion needs to be met when determining Δt in the implicit method. However, to properly model transient phenomena, it is necessary to set Δt at least one order of magnitude smaller than the smallest time scale in the system being modeled (Fluent 6.3 User's Guide). Usually, the time step size Δt is determined by trial and error. A good way to choose Δt is to look at the number of iterations it takes Fluent to converge at each time step. The ideal number of iterations per time step is 5-10.

In addition to the trial and error method, it is also possible to calculate the time step size based on the Courant number. The Courant number is a dimensionless number that compares the time step in a calculation to the characteristic time of transit of a fluid element through a control volume as follows.

$$CFL = \frac{\Delta t}{\Delta x_{cell}/v_{fluid}} \tag{10}$$

Therefore, if a common value for the Courant number or CFL condition as 0.25 is chosen, the order of the time step can be obtained by dividing the order of the characteristic length of the interface elements by the order of the free surface velocity, such as

$$\Delta t = CFL \frac{\Delta x_{cell}}{v_{fluid}} \approx 0.25 \frac{0.001}{1} = 2.5 \times 10^{-4} \tag{11}$$

4. RESULTS AND DISCUSSION

In order to better investigate the effect of various factors on the formation of the vortex, the numerical results are presented in several sections as follows.

4.1 Validation of the Results

In this section, the results of the solution for the tangential velocity are compared with existing analytical relations for the verification of the accuracy of the numerical simulation. For this purpose, the analytical solution of Odgaard (1986) and the relation provided by Wang et al. (2011), shown in Eqs. (12) and (13), have been selected.

$$v_\theta = \frac{\Gamma}{2\pi r}[1 - exp(-1.25\bar{r}^2)] \tag{12}$$

$$v_\theta = \frac{\Gamma}{2\pi r_m}\frac{0.928\bar{r}}{1 - 0.7\bar{r} + \bar{r}^2} \tag{13}$$

where $\bar{r} = r/r_m$ and r_m is the radius at which the maximum tangential velocity occurs. Also, Γ is circulation. Equations (12) and (13) have been obtained for fluid motion that is steady, axisymmetric, incompressible, and laminar (Odgaard, 1986; Wang et al.,

2011). The same equations are used for turbulent flow except that the molecular viscosity is replaced with effective viscosity wherever needed. If the tangential velocity becomes normalized with its maximum values, the following two dimensionless relations will be obtained.

$$\frac{v_\theta}{v_{\theta m}} = \frac{1.4}{\bar{r}}[1 - exp(-1.25\bar{r}^2)] \qquad (14)$$

$$\frac{v_\theta}{v_{\theta m}} = 1.3 \frac{\bar{r}}{1 - 0.7\bar{r} + \bar{r}^2} \qquad (15)$$

The numerical results for the normalized tangential velocity in both laminar and turbulent flows corresponding to Run1 and Run3 in Table 3 are shown in Figures 5 and 6 respectively. As can be seen, there is reasonable agreement between the two plots, especially for laminar flow. For turbulent flow, however, the amount of error in the free vortex region is more significant.

A weakness of the analytical relationships, at least for confined boundary flow domains such as the present tank, is their near-wall behavior. As can be deduced from Eqs. (10) and (11) and shown in Figures 5 and 6, the tangential velocity at the tank wall is not zero (Wang et al., 2011; Azarpira & Zarrati, 2019). In other words, the no-slip condition in these relations occurs infinitely, which is inconsistent with most real geometries. This weakness of the analytical relations leads to more errors between the values obtained from these relations and the numerical results near the wall, which will be discussed in Section 3.7.
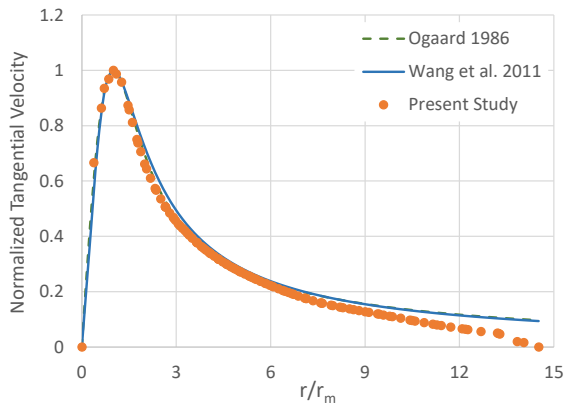
Fig. 5 Comparison of the present numerical solution for laminar flow with the analytical solutions
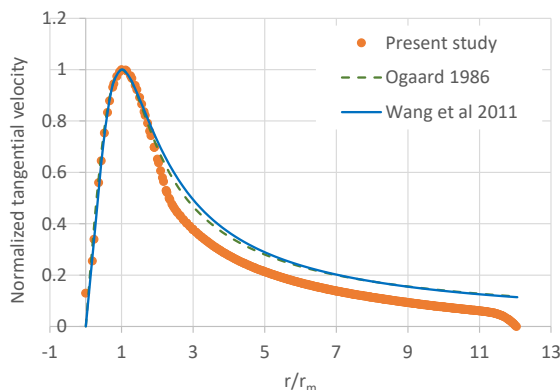
Fig. 6 Comparison of the present numerical solution for turbulent flow with the analytical solutions

4.2 Effect of discharge time and depth on velocity components

Figures 7 to 10 show the values of the velocity components, i.e., axial velocity, tangential velocity, and radial velocity, as well as the pressure along the four lines shown in Fig. 1 for Run 4 at time 1 Sec. This has been done to show the effect of depth and proximity of the flow to the tank outlet on vortex formation.
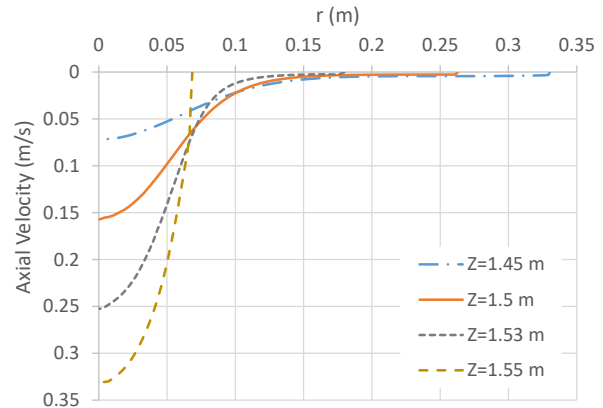
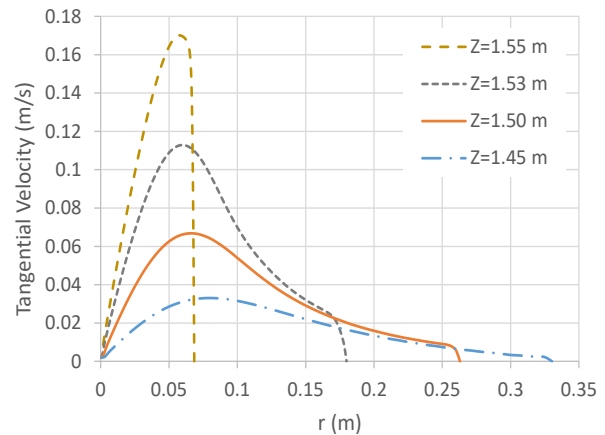**Fig. 7 Comparison of axial velocity changes along the four lines shown in Figure 1 and t=1 sec**

Fig. 8 Comparison of tangential velocity changes along the four lines shown in Figure 1 at t=1 sec
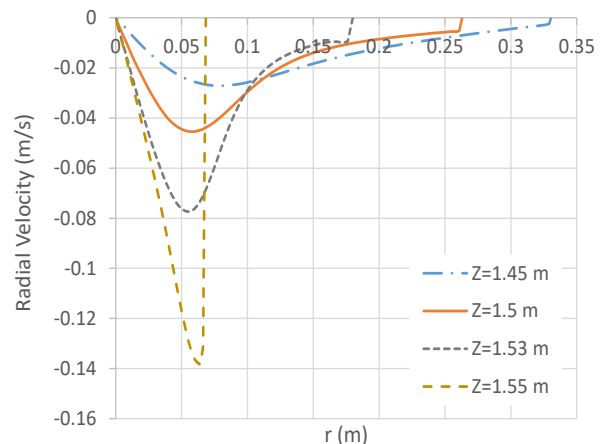
Fig. 9 Comparison of radial velocity changes along the four lines shown in Fig. 1 at t=1 sec
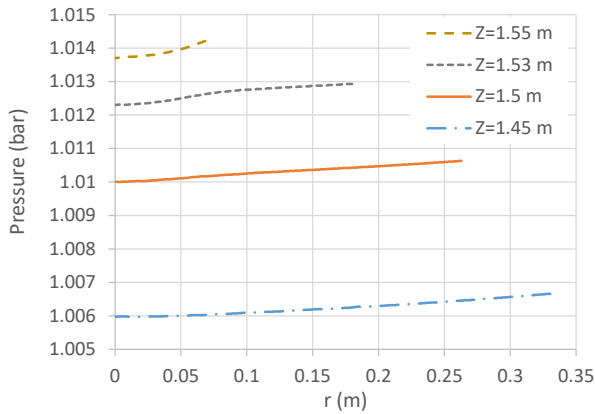
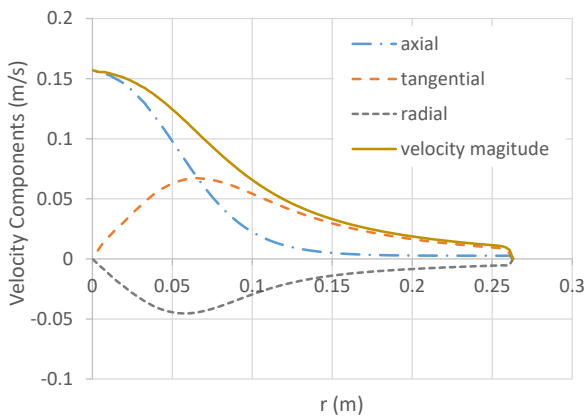Fig. 10 Comparison of pressure changes along the four lines shown in Fig. 1 at t=1 sec

Fig. 11 Variations of velocity components and velocity magnitude along the line z=1.5 m at t=1 sec
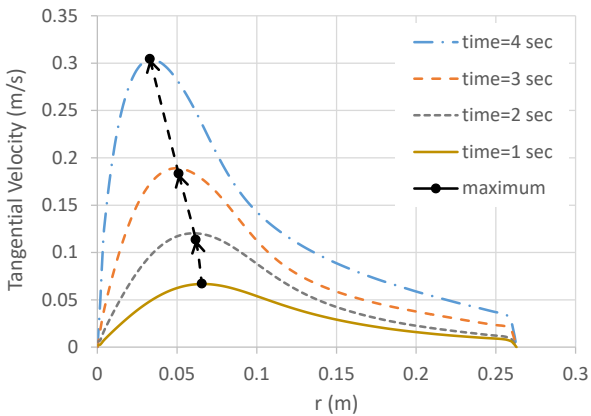

Fig. 12 Effect of time passage on the tangential velocity along line z=1.5 m

It can be seen from Figures 7 to 10 that all three velocity components increase as the flow approaches the tank outlet. For the pressure (Fig. 10), although its value increases with depth, it leaves the horizontal straight line state as it approaches the tank outlet and decreases as it moves away from the wall towards the tank axis. It can also be seen from Figures 8 and 9 that the behavior of the tangential and radial velocity components is very similar, except that the value of the radial velocity is negative. Figure 11 compares the three axial, tangential, and radial velocity components together with the velocity
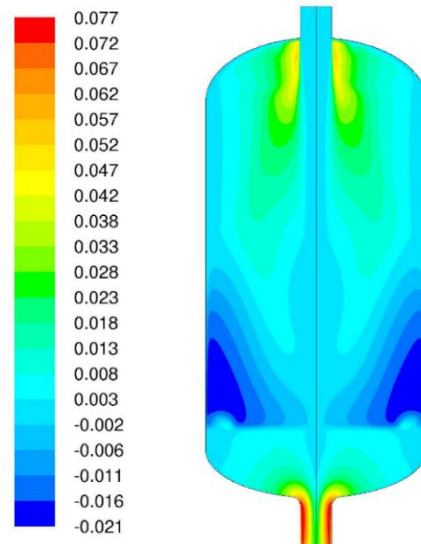
(a) Ω=0.1 rad/s
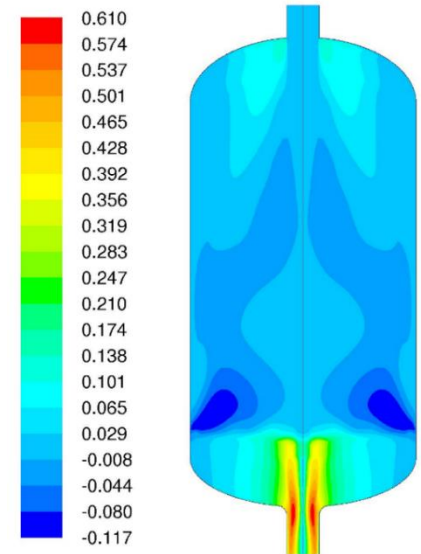
(b) Ω=1 rad/s

Fig. 13 Effect of the angular velocity of the reference frame on tangential velocity (m/s)

magnitude. It can be seen that the velocity magnitude is more affected than the axial velocity component. Accordingly, its maximum occurs on the axis of the tank. As time passes and the vortex intensity increases, the maximum velocity occurs where the maximum tangential velocity occurs. Figure 12 examines the effect of time on the tangential velocity at a given depth, z=1.5 m. It can be seen from Fig. 12 that at a given depth, the vortex strength increases as time passes and the liquid level decreases. Also, the maximum tangential velocity, initially outside the cross-section of the outlet pipe, i.e. r=0.05 m, moves towards the center of the vortex flow (dotted line).

4.3 Effect of the Angular Velocity of Reference Frame

This section examines the effect of the angular velocity of the reference frame on the flow characteristics. For this purpose, two angular velocities of 0.1 and 1 rad/s have been applied, with all other conditions held constant. The results for the tangential velocity contours are shown in Fig. 13.
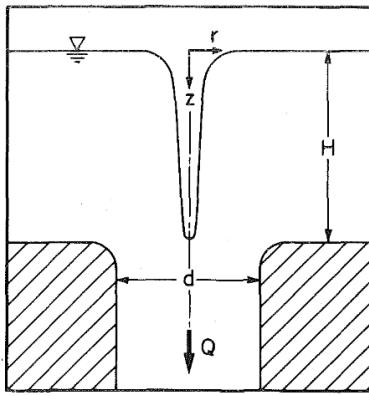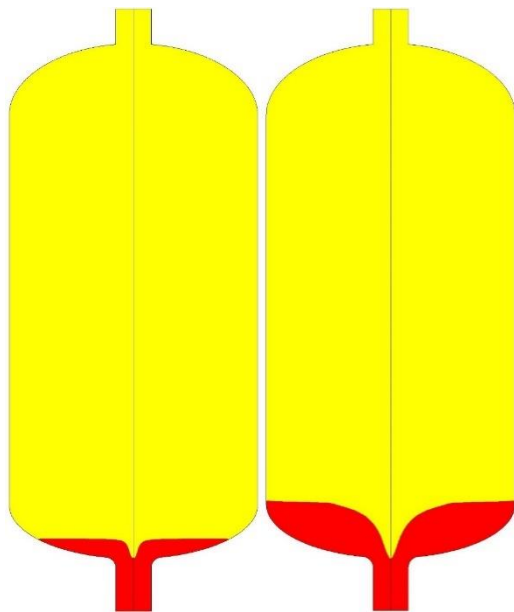
Fig. 14 The schematic of critical height in a free-surface flow (Odgaard, 1986)
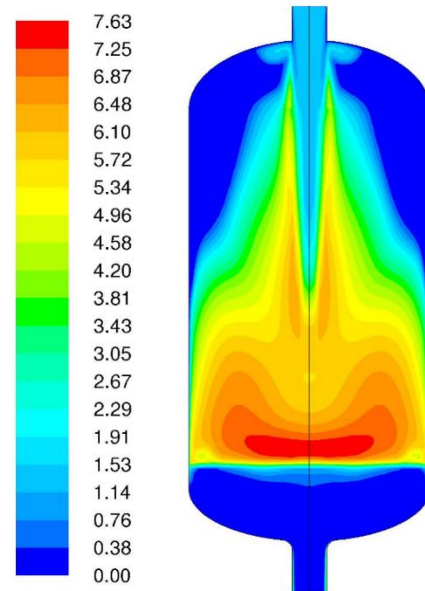

(a) Ω=0.1 rad/s

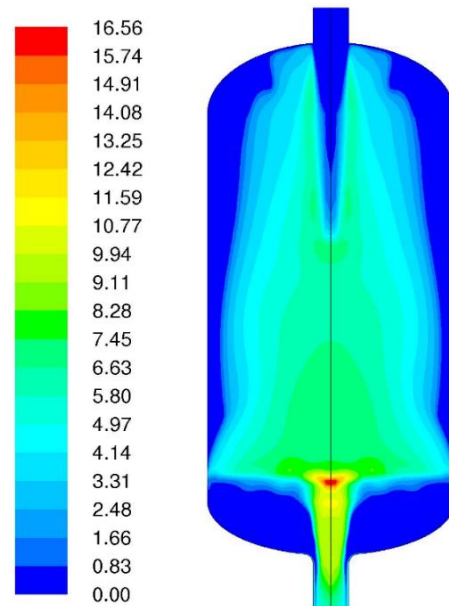(a) Ω=0.1 rad/s and t=23.4 sec   (b) Ω=1 rad/s and t=12.75 sec

Fig. 15 Effect of the angular velocity of the reference frame on the gas-liquid interface

(b) Ω=1 rad/s

Fig. 16 Effect of the angular velocity of the reference frame on turbulence intensity (%)

It can be seen that when the angular velocity is 1 rad/s, the region where the tangential velocity is significant is drawn from the surface of the liquid to the outlet of the pipe. Moreover, its magnitude is much higher than in the other case. On the other hand, for the case, Ω=0.1 rad/s, the height of the significant tangential velocity is approximately from the bottom of the tank to the end of the outlet pipe. Higher angular velocities also affect the critical height. The critical height, H, as shown in Fig. 14, is defined as the distance from the free surface when the tip of the air core reaches the pipe inlet.

Figure 15 (a and b) shows the effect of angular velocity on the gas-liquid interface for a state where the critical height has been reached. The results show that for the case where the angular velocity is 0.1 rad/s, Fig 15.a, the time for the air core to reach the inlet of the pipe is 23.4 seconds, while for the case where the angular velocity is 1 rad/s, Fig 15.b, this time is reduced to 12.75 seconds. Since

the outflow of liquid from the tank is known, the mass of the remaining liquid is 8.23 kg in the first case and 40.18 kg in the second. Note that the initial mass of the liquid in the tank is 78.43 kg.

In addition to vortex characteristics such as tangential velocity, changing the angular velocity also affects other flow properties. For example, the turbulence intensity contours for the two states are shown in Fig. 16 (a and b). While the value of this quantity for Ω=0.1 rad/s is only noticeable in the gas region, for Ω=1 rad/s it has significant values in the central core of the vortex. Moreover, its magnitude is much higher than in the other case. Turbulence intensity is generally defined as the ratio of velocity fluctuations to a reference velocity. For an

isotropic turbulent flow, this quantity can be related to the turbulent kinetic energy, k, as follows.

$$I = \frac{\sqrt{2/3\,\rho k}}{U_{ref}} \tag{16}$$

In Eq. (16), *I* is turbulence intensity, k is turbulent kinetic energy, ρ is the fluid density, and U_{ref} is reference velocity.

4.4 Effect of Air Pressure

In some applications, such as spacecraft, the tank gas pressure is higher than the normal atmospheric pressure (Karimi et al., 2010). Therefore, this section investigates the effect of this parameter on the vortex formation in the tank outlet. For this purpose, the simulation is performed once for the air pressure of 1 bar and another time for the air pressure of 5 bar, corresponding to Run 4 and Run 5. Other simulation conditions are considered in the same way.

The present numerical results show that the change in air pressure does not affect the vortex formation mechanism in the initial moments of the simulation. However, after about 3.5 seconds from the start of the discharge, changes occur in the tangential and axial velocity components, as shown in Figures 17 and 18. These changes are most pronounced near the centerline of the vortex. These differences between the two states are probably due to the velocity and direct impact of the incoming air on the liquid surface, which causes the vortex to form more quickly. The free surface profiles for the two states mentioned are shown in Fig. 19 (a and b) for better comparison. To keep the air pressure constant at 5 bar, the inlet air flow rate is set to 0.0175 kg/s. According to the cross-section of the tank inlet pipe, this mass flow rate corresponds to a velocity of about 0.385 m/s.

To see the pressure changes inside the tank, the pressure contour for the case with p=5 bar at 5 seconds from the start of tank emptying is shown in Fig. 20. The pressure gradient in the gas section and the constant pressure lines in the vortex flow section are clearly defined.
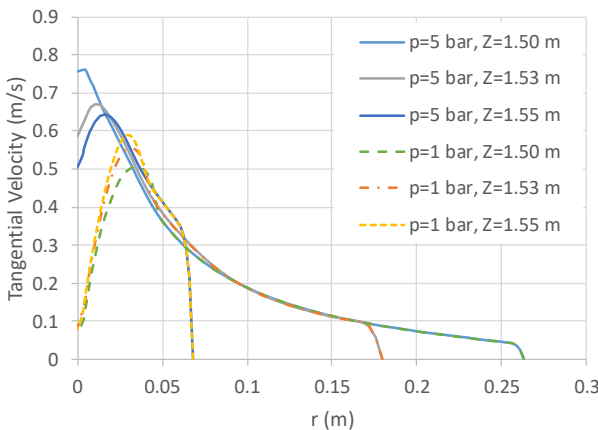

Fig. 18 Effect of air pressure on the axial velocity at different tank cross-sections at t=5 sec
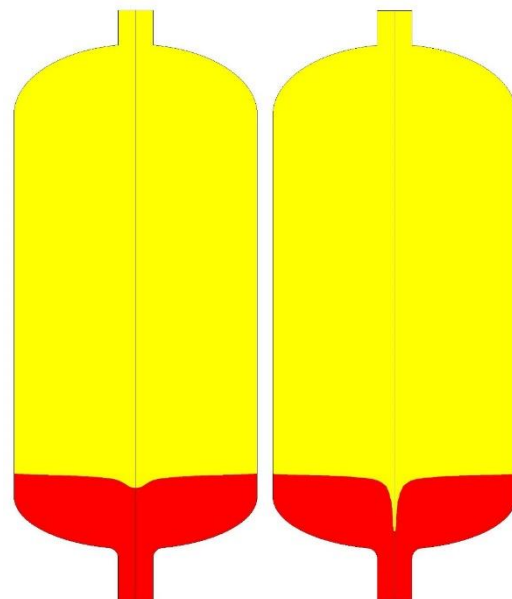
(a) p=1 bar   (b) p=5 bar
Fig. 19 Effect of gas pressure on the gas-liquid interface at t=5 sec

Fig. 17 Effect of air pressure on the tangential velocity at different cross-sections of the bottom of the tank at t=5 sec
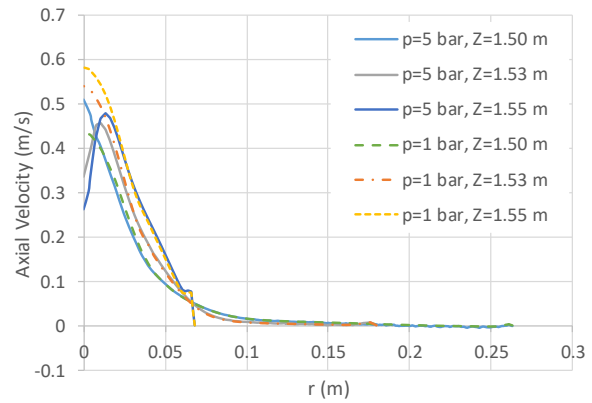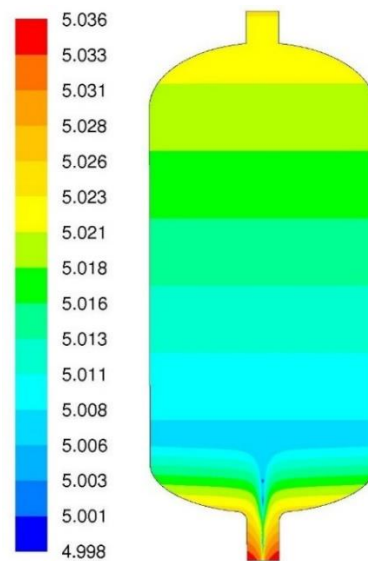

Fig. 20 The contour of absolute static pressure (bar) for Run 5 of Table 3 at time=5 sec

4.5 Turbulent viscosity variations

Most industrial flows, including vortices, are in a turbulent regime. One of the most common methods used to model this flow is the Reynolds time-averaging method, which in most cases, uses a quantity called turbulent viscosity or eddy viscosity. Models such as k-ε or k-ω are of this type. The turbulent viscosity is one of the turbulent flow properties that varies from one point to another within the flow. However, in the analytical solution of turbulent vortex flows, this quantity is considered a constant value for each flow condition, two examples of which are given in Eqs. (17) and (18) (Hite & Mih, 1994; Azarpira & Zarrati, 2019). These values are used for both axial and radial velocity components in the analytical relations of the vortex flow.

$$\varepsilon = \frac{Q}{4\pi d} \tag{17}$$

$$\nu_{eff,r_m} = \nu + \varepsilon = \frac{1.4Q}{8\pi H} \tag{18}$$

In the above relations, ε is the eddy viscosity, $\nu_{eff,rm}$ is effective eddy viscosity, ν is the kinematic viscosity of the fluid, Q is the outlet flow rate, d is the diameter of the outlet pipe, and H is the height of the free surface to the inlet of the pipe. Based on the above relations and the conditions of the present study, the amount of turbulent viscosity is equal to the following values.

$$\varepsilon = 0.00239 \ m^2/s \ and \ \nu_{eff,r_m} = 0.000836 \ m^2/s$$

It should be noted that similar to the kinematic viscosity of a fluid, the turbulent kinematic viscosity or eddy viscosity is obtained by dividing the viscosity by the density of the fluid. The sum of the turbulent and molecular viscosities is also called the effective viscosity, ν_{eff}. Furthermore, in most central regions of the flow, the magnitude of ε is much more significant than ν. So it can be written $\nu_{eff} \approx \varepsilon$. Figure 21 (a and b) shows the contours of ν_{eff} for the two angular velocities of Ω=0.1 rad/s and Ω=1 rad/s, respectively. As can be seen, the value of turbulent viscosity is significant only in the center of the vortex flow, and in other places, due to the low-velocity gradient of the fluid, its value is insignificant. In addition, the value of this quantity varies with position in the flow and, of course, with time.

For a more precise observation, the effective turbulent viscosity changes for the two states corresponding to Fig. 21 are plotted in Figures 22 and 23, respectively. It is observed that only for Ω=1 rad/s, where the turbulence is more intense, the amount of effective turbulent viscosity in some regions is comparable to the values obtained from Eqs. (17) and (18). It can be concluded that these relations can be used only for specific situations.

4.6 The near-wall behavior of analytical relations

As can be seen in Figures 5 through 9, the no-slip condition at the wall causes the three velocity components, including the tangential velocity, to reach zero at the wall. On the other hand, all analytical solutions predict a non-zero value for the tangential velocity at the wall. Figure 24 shows the normalized tangential velocity plots based on well-known analytical relationships. Two of these
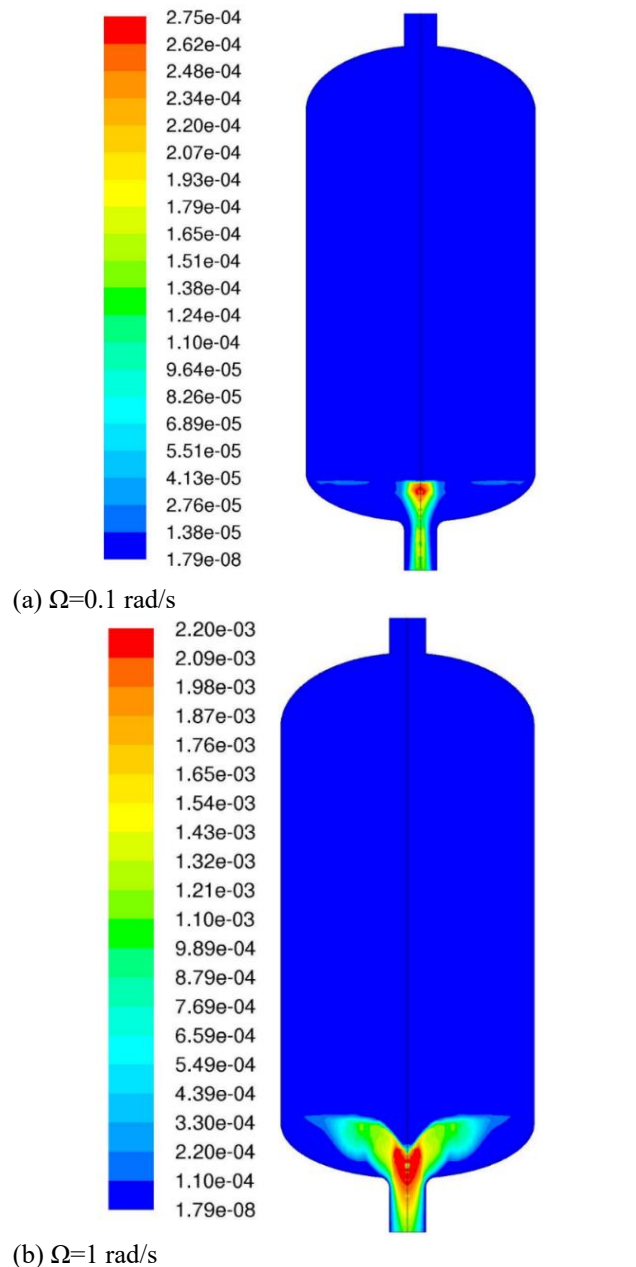
(a) Ω=0.1 rad/s

(b) Ω=1 rad/s

Fig. 21 Effective turbulent viscosity contour (m²/s) for two angular velocities

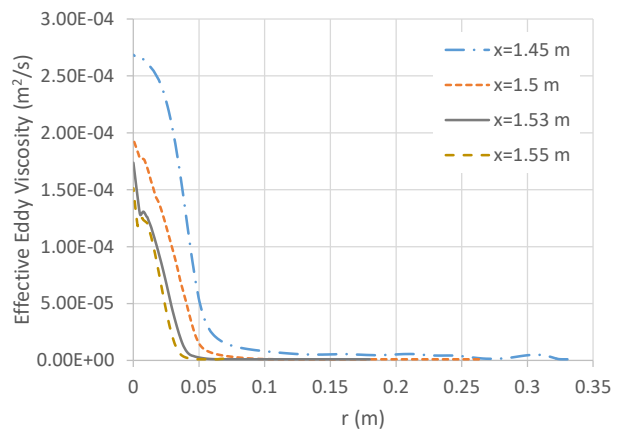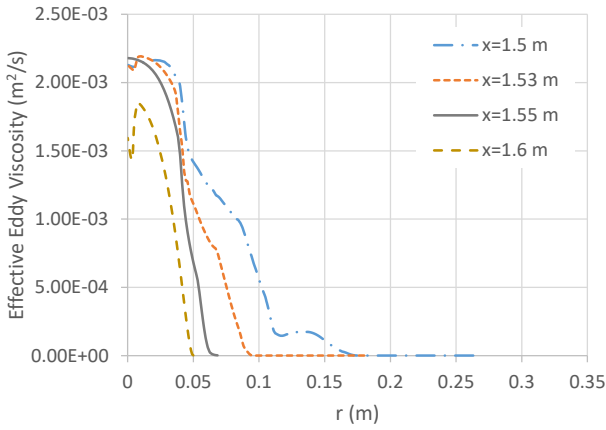**Fig. 22 Variations of effective turbulent viscosity for Ω=0.1 rad/s**

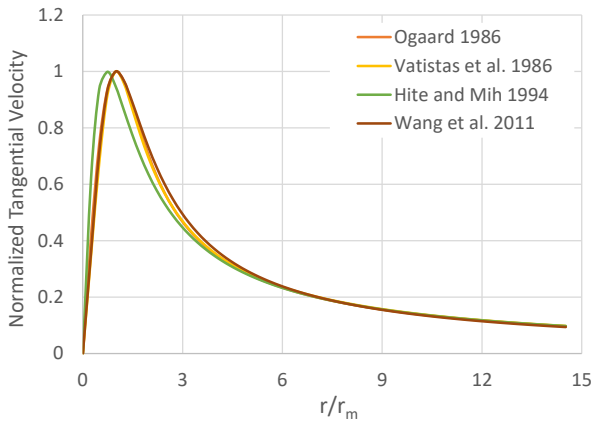**Fig. 23 Variations of effective turbulent viscosity for Ω=1 rad/s**

Fig. 24 Variations of normalized tangential velocity based on some analytical relations

relations are already given in Eqs. (12) and (13) (Odgaard, 1986; Wang et al., 2011), and the other two are given in Eqs. (19) and (20) (Vatistas et al., 1991; Hite & Mih, 1994).

$$v_\theta = \frac{\Gamma}{2\pi r_m} \frac{\bar{r}}{(1 + \bar{r}^4)^{0.5}} \tag{19}$$

$$v_\theta = \frac{\Gamma}{2\pi r_m} \frac{2\bar{r}}{1 + 2\bar{r}^2} \tag{20}$$

Therefore, this section attempts to correct the existing relationships based on the boundary layer theory (Fox et al., 2020). Figure 25 shows the changes in the velocity profile in the boundary layer near the wall, ranging from zero at the wall to a free flow velocity at the edge of the boundary layer, δ.

The results of the present numerical solution for the tangential velocity show that, depending on the flow conditions, the thickness of the boundary layer is about 5~10% of the tank radius. The lower limit is for laminar flow and the upper limit is for turbulent flow. Therefore, in order to consider the no-slip condition on the wall, one of the mentioned previous relations for the tangential velocity, for example, Ogaard's relation, is rewritten as follows.
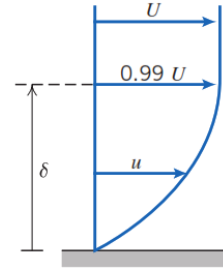

Fig. 25 Schematic of velocity profiles near the wall inside the boundary layer (Fox et al., 2020)

$$\bar{u}_\theta = \frac{u_\theta}{u_{\theta m}} = \frac{1.4}{\bar{r}}[1 - exp(-1.25\bar{r}^2)] , \bar{R} < 0.9 \tag{21}$$

where $\bar{r} = r/r_m$ and $\bar{R} = r/R$

For the range $0.9 \leq \bar{R} \leq 1$ the following second-degree polynomial is used for the velocity profile inside the boundary layer.

$$\bar{u}_\theta = a + b\bar{R} + c\bar{R}^2 \tag{22}$$

The constants of this profile can be calculated from the following three conditions.

$$\begin{cases} \bar{R} = 1 : \bar{u}_\theta = 0 \\ \bar{R} = 0.9 : \bar{u}_\theta = V_\theta \\ \bar{R} = 0.9 : \partial\bar{u}_\theta/\partial\bar{R} = 0 \end{cases} \tag{23}$$

The value of V_θ in the above condition is obtained from Eq. (21) for $\bar{R} = 0.9$.

After solving the system of the above three equations and three unknowns, the values of constants a, b, and c are obtained as follows.

$$\begin{cases} a = -80V_\theta \\ b = 180V_\theta \\ c = -100V_\theta \end{cases} \tag{24}$$

This method can be used for all of the analytical tangential velocity relationships presented, i.e., Eqs. (12), (13), (19), and (20). Accordingly, the modified tangential velocity plots are shown in Figure 26. Also, in Fig. 27 and 28, the correction made to Ogaard's relation is compared with the results of the present numerical solution. As can be seen, the modification correctly follows the behavior of the numerical data near the wall.
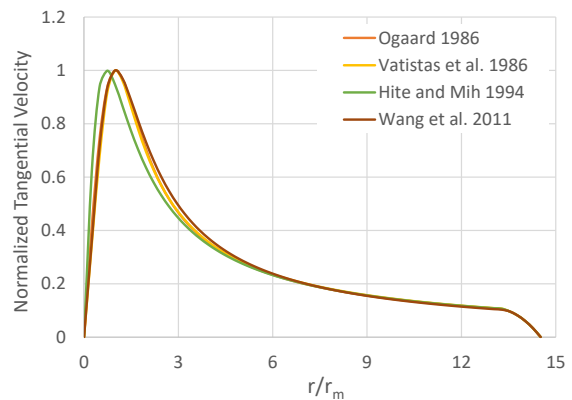

Fig. 26 Effect of no-slip condition on analytical relations for tangential velocity.
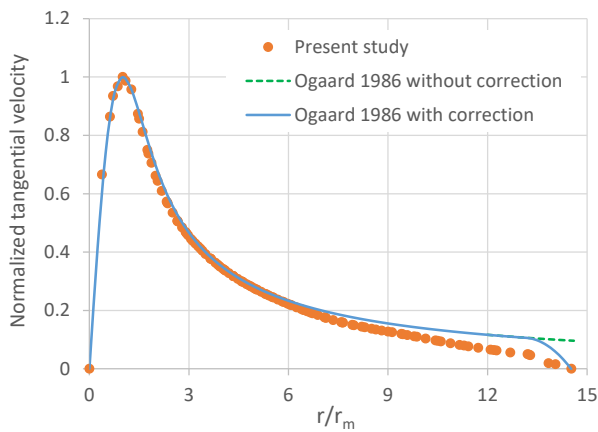
Fig. 27 Effect of no-slip condition on Odgaard's relations for tangential velocity in laminar flow and comparison with the present numerical study
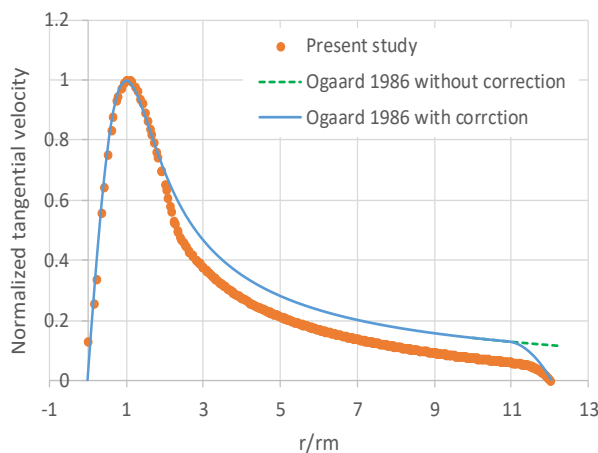

Fig. 28 Effect of no-slip condition on Odgaard's relations for tangential velocity in turbulent flow and comparison with the present numerical study

5. CONCLUSION

In this research, the vortex formation at the outlet of a tank has been studied transiently by numerical method. The effect of some influencing factors such as air pressure, reference frame rotation, liquid depth, and discharge time on the vortex formation has been studied. In addition, the near-wall behavior of the analytical relations for tangential velocities and the relations presented for turbulent viscosity have also been verified. The main results of this research are as follows:

1. Increasing the angular velocity of the reference frame from 0.1 to 1 rad/s increases the maximum tangential velocity by about 10 times, increasing the height of its formation region from the liquid surface to the end of the tank outlet pipe. However, at an angular velocity of 0.1 rad/s, vortex formation is generally confined to the bottom of the tank and inside the outlet tube. Furthermore, at an angular velocity of 1 rad/s, the critical height occurs at approximately 12.75 seconds after the liquid is discharged, whereas, at a velocity of 0.1 rad/s, it occurs at 23.4 seconds. In other words, the mass of liquid remaining at the bottom of the tank in the first case, i.e. $\Omega=1$ rad/s, is approximately 32 kg more

than in the second case. Other flow characteristics, such as the intensity of the turbulence in the central part of the vortex, also change significantly.

2. The change of the gas pressure from 1 to 5 bar, and possibly the direct contact of the gas with the liquid surface, speeds up the process of vortex formation and critical height considerably. In other words, at a pressure of 1 atmosphere, the critical height occurs approximately 12.75 seconds after the discharge process, whereas, at a pressure of 5 bar, this time is reduced to approximately 5.5 seconds. For the conditions of the present study, this means a difference in liquid mass of 21.75 kg.

3. Using the boundary layer theory and applying the no-slip condition to the wall, the near-wall behavior of the analytical relations for the tangential velocity has been modified. This modification means that the magnitude of the velocity in the near-wall region is gradually reduced to zero at the wall.

4. The study of the changes in turbulent viscosity in the present numerical simulation has shown that its value is significantly different from the constant value given by the semi-empirical relations and that this difference varies with time. Given the nature of this quantity and its variability, the use of these relations can lead to significant errors in the analytical results.

5. It was observed that in the lower layers of the liquid, the magnitude of the velocity components increases as it approaches the outlet pipe inlet. Also, at a certain point in the bottom of the tank, the magnitude of the velocity components increases with time and as the liquid level decreases.

In this research, the shape, dimensions, and boundary conditions of the reservoir and the two gas and liquid fluids have been chosen arbitrarily. Nevertheless, it can be solved in desired conditions and specific applications. However, the following topics are suggested for future research.

- Use the diffuser at the tank's inlet to disperse the air and examine its effect on vortex characteristics.

- Applying different turbulence models to compare their performances.

- Accurate estimation of the boundary layer thickness to modify the tangential velocity profile.

CONFLICT OF INTEREST

The authors declare that they have no known competing financial interests or personal relationships that could have appeared to influence the work reported in this paper.

AUTHORS CONTRIBUTION

Material preparation, data collection, analysis, and drafting of the manuscript were performed by M.

Mohseni. Investigation and critical review of the manuscript were performed by M.K. Domfeh.

REFERENCES

Agarwal, D., Basu, P., Tharakanc, T. J., & Salihd, A. (2014). Prediction of gas-core vortices during draining of liquid propellants from tanks. *Aerospace Science and Technology,* 32, 60–65. https://doi.org/10.1016/j.ast.2013.12.001

Ahn, S. H., Xiao, Y., Wang, Z., Luo, H., & Luo, Y. (2019). Numerical estimation of air core length in two-phase free surface vortex. *Journal of Hydraulic Research*, 57 (4), 475-487. https://doi.org/10.1080/00221686.2018.1489899

Azarpira, M., & Zarrati, A. R. (2019). A 3D analytical model for vortex velocity field based on spiral streamline pattern. *Water Science and Engineering,* 12 (3), 244-252. https://doi.org/10.1016/j.wse.2019.09.001

Basu, P., Agarwal, D., Tharakan, T. J., & Salih, A. (2013). Numerical studies on air-core vortex formation during draining of liquids from tanks. *International Journal of Fluid Mechanics Research,* 40 (1), 27-41. https://doi.org/10.1615/InterJFluidMechRes.v40.i1.30

Domfeh, M. K., Gyamfi, S., Amo-Boateng, M., Andoh, R., Ofosu, E. A., & Tabor, G. (2020a). Numerical simulation of an air-core vortex and its suppression at an intake using openFOAM. *Fluids,* 5, 221. https://doi.org/10.3390/fluids5040221

Domfeh, M. K., Gyamfia, S., Amo-Boateng, M., Andoh, R., Ofosu, E. A., & Tabor, G. (2020b). Free surface vortices at hydropower intakes: A state-of-the-art review. *Scientific African,* 8 e00355. https://doi.org/10.1016/j.sciaf.2020.e00355

Fluent 6.3 User's Guide, Copyright 2006 by Fluent Inc.

Fox, R. W., McDonald, A., & Mitchell, J. (2020). *Fox and McDonalds: Introduction to Fluid Mechanics* (10th Ed.). John Wiley & Sons Inc.

Hite, J. E., & Mih, W. C. (1994). Velocity of air-core vortices at hydraulic intakes. *Journal of Hydraulic Engineering,* 120 (3), 284–297. https://doi.org/10.1061/(ASCE)0733-9429(1994)120:3(284)

Huang, T. H. , Jan, C. D., & Hsu, Y. C. (2017). Numerical simulations of water surface profiles and vortex structure in a vortex settling basin by using Flow-3D. *Journal of Marine Science and Technology,* 25 (5), 531-542. https://doi.org/10.6119/JMST-017-0509-1

Jochmann, P., Sinigersky, A., Hehle, M., Scha¨fer, O., Koch, R., & Bauer, H. J. (2006). Numerical simulation of a precessing vortex breakdown. *International Journal of Heat and Fluid Flow,* 27, 192–203. https://doi.org/10.1016/j.ijheatfluidflow.2005.08.003

Kabiri-Samani, A. R., & Borghei, S. M. (2013). Effects of anti-vortex plates on air entrainment by free vortex. *Scientia Iranica,* 20(2), 251–258. https://doi.org/10.1016/j.scient.2012.10.041

Kan, K., Xu, Y., Li, Z., Xu, H., Chen, H., Zi, D., Gao, Q., & Shen, L. (2023). Numerical study of instability mechanism in the air-core vortex formation process. *Engineering Applications of Computational Fluid Mechanics*, 17(1), 2156926. https://doi.org/10.1080/19942060.2022.2156926

Karimi, H., Nassirharand, A., & Mohseni, M. (2010). Modeling and simulation of a class of liquid propellant engine pressurization systems. *Acta Astronautica,* 66, 539-549. https://doi.org/10.1016/j.actaastro.2009.07.018

Li, J., Liang, G., Zhu, P., & Wang, X. (2019). Numerical investigation of the operating process of the liquid hydrogen tank under gaseous hydrogen pressurization. *Aerospace Science and Technology,* 93, 105327. https://doi.org/10.1016/j.ast.2019.105327

Mahyari, M. N. , Karimi, H., Naseh H. & Mirshams, M. (2010). Numerical and experimental investigation of vortex breaker effectiveness on the improvement in launch vehicle ballistic parameters. *Journal of Mechanical Science and Technology,* 24 (10), 1997-2006. https://doi.org/10.1007/s12206-010-0618-7

Manda, U., Parahovnik, A., & Peles, Y., (2020). Theoretical *Investigation of boundary layer behavior and heat transfer of supercritical carbon dioxide (sCO2) in a microchannel*. 19th IEEE Intersociety Conference on Thermal and Thermomechanical Phenomena in Electronic Systems (ITherm), Orlando, FL, USA. https://doi.org/10.1109/ITherm45881.2020.9190408

Manda, U., Parahovnik, A., & Peles, Y., (2022). Thermoacoustic waves and Piston Effect inside a microchannel with Carbon Dioxide near critical conditions. *Thermal Science and Engineering Progress,* 36(1), Article 101528. https://doi.org/10.1016/j.tsep.2022.101528

Manda, U., Parahovnik, A., Mazumdar, S., & Peles, Y., (2023). Heat transfer characteristics of turbulent flow of supercritical carbon dioxide (sCO2) in a short-heated microchannel. *International Journal of Thermal Sciences*, 192, Part A, Article 108389, https://doi.org/10.1016/j.ijthermalsci.2023.108389.

Manda, U., Peles, Y., & Putnam, S. (2021). *Comparison of heat transfer characteristics of flow of supercritical carbon dioxide and water inside a square microchannel*. 20th IEEE Intersociety Conference on Thermal and Thermomechanical Phenomena in Electronic Systems (iTherm), San Diego, CA, USA. https://doi.org/10.1109/ITherm51669.2021.950319.

Monshizadeh, M., Tahershamsi, A., Rahimzadeh, H., & Sarkardeh, H. (2018). Vortex dissipation using a hydraulic-based anti-vortex device at intakes.

International Journal of Civil Engineering, 16, 1137–1144. https://doi.org/10.1007/s40999-017-0266-8

Mulligan, S., Casserly, J., & Sherlock, R. (2014). Advances in Hydroinformatics. In P. Gourbesville, J. A. Cunge and G. Caignaert (Eds.), *Springer Water* (pp. 549-569). Experimental and Numerical Modelling of Free-Surface Turbulent Flows in Full Air-Core Water Vortices https://doi.org/10.1007/978-981-287-615-7_37

Naderi, V., Farsadizadeh, D., Lin, C., & Gaskin, S. (2019). A 3D study of an Air-Core vortex using HSPIV and flow visualization. *Arabian Journal for Science and Engineering*, 44, 8573–8584. https://doi.org/10.1007/s13369-019-03764-3

Odgaard, A. J. (1986). Free-surface air core vortex. *Journal of Hydraulic Engineering,* 112 (7), 610–620. https://doi.org/10.1061/(ASCE)0733-9429(1986)112:7(610)

Sarkardeh, H. (2017). Numerical calculation of air entrainment rates due to intake vortices. *Meccanica*, 52, 3629–3643. https://doi.org/10.1007/s11012-017-0687-0

Suerich-Gulick1, F., Gaskin, S. J., Villeneuve, M., & Parkinson, É. (2014). Free surface intake vortices: theoretical model and measurements. *Journal of Hydraulic Research*, 52 (4). https://doi.org/10.1080/00221686.2014.896425

Sun, H., & Liu, Y. (2015). Theoretical and experimental study on the vortex at hydraulic intakes. *Journal of Hydraulic Research,* 53 (6), 787–796. https://doi.org/10.1080/00221686.2015.1076533

Taştan, K., & Yildirim, N. (2014). Effects of froude, reynolds, and weber numbers on an air-entraining vortex. *Journal of Hydraulic Research,* 52 (3), 421–425. https://doi.org/10.1080/00221686.2013.879541

Tayyab, M., Cheema, T. A., Malik, M. S., Muzaffar, A., Sajid, M. B., & Park, C. W. (2020). Investigation of thermal energy exchange potential of a gravitational water vortex. *Renewable Energy,* 162, 1380-1398. https://doi.org/10.1016/j.renene.2020.08.097

Thingbø, S. S. (2013). *Simulation of viscous flow around a circular cylinder with STAR-CCM+*. [Master Thesis, Norwegian University of Science and Technology]. Marine Hydrodynamics. http://hdl.handle.net/11250/238639

Trivellato, F. (2010). Anti-vortex devices: Laser measurements of the flow and functioning. *Optics and Lasers in Engineering*, 48, 589–599. https://doi.org/10.1016/j.optlaseng.2009.11.010

Vatistas, G. H., Kozel, V. & Mih, W. C. (1991). A simpler model for concentrated vortices. *Experiments in Fluids,* 11 (1), 73–76. https://doi.org/10.1007/BF00198434

Versteeg, H. K., & Malalasekera, W. (2007). *An introduction to computational fluid dynamic, the finite volume method* (2nd ed.). Pearson Education Limited.

Wang, Y., Jiang, C., & Liang, D. (2011). Comparison between empirical formulae of intake vortices. *Journal of Hydraulic Research,* 49 (1), 113–116. https://doi.org/10.1080/00221686.2010.534279

Zi, D., Shen, L., Wang, F., Wang, B., & Yao, Z. (2022). Characteristics and mechanisms of air-core vortex meandering in a free-surface intake flow. *International Journal of Multiphase Flow,* 152, Article 104070. https://doi.org/10.1016/j.ijmultiphaseflow.2022.104070

Zi, D., Wang, F., Wang, C., Huang, C., & Shen, L. (2021). Investigation on the air-core vortex in a vertical hydraulic intake system. *Renewable Energy,* 177, 1333-1345. https://doi.org/10.1016/j.renene.2021.06.062

Zi, D., Xuan, A., Wang, F., & Shen, L. (2020). Numerical study of mechanisms of air-core vortex evolution in an intake flow. *International Journal of Heat and Fluid Flow,* 81, Article 108517. https://doi.org/10.1016/j.ijheatfluidflow.2019.108517

Zuo, Z., Jiang, W., Qin, X., & Huang, Y. (2021). A numerical model for liquid–vapor transition in self-pressurized cryogenic containers. *Applied Thermal Engineering,* 193, Article 117005. https://doi.org/10.1016/j.applthermaleng.2021.117005.